



Characteristics of Landsat 8 OLI-derived NDVI by comparison with multiple satellite sensors and in-situ observations



Yinghai Ke^a, Jungho Im^{b,*}, Junghee Lee^b, Huili Gong^a, Youngryel Ryu^c

^a College of Resource Environment and Tourism, Capital Normal University, Beijing, China

^b School of Urban and Environmental Engineering, Ulsan National Institute of Science and Technology (UNIST), Ulsan, South Korea

^c Department of Landscape Architecture and Rural Systems Engineering, Seoul National University, Seoul, South Korea

ARTICLE INFO

Article history:

Received 25 November 2014

Received in revised form 3 March 2015

Accepted 3 April 2015

Available online 23 April 2015

Keywords:

NDVI

Landsat OLI

Landsat ETM+

MODIS

GOCI

Light emitting diodes

ABSTRACT

Vegetation indices are important remotely sensed metrics for ecosystem monitoring and land surface process assessment, among which Normalized Difference Vegetation Index (NDVI) has been most widely used. The newly launched Landsat 8 Operational Land Imager (OLI) sensor, together with its predecessor Landsat 7 Enhanced Thematic Mapper Plus (ETM+), provides continuous earth observations with an 8-day interval. The design improvements of the new sensor, including narrower near-infrared waveband, higher signal-to-noise ratio (SNR), and greater radiometric sensitivity highlight the need for investigating the land surface observation properties, especially its consistency with data from its predecessors and other satellite sensors. This study aims to evaluate the characteristics of Landsat 8 OLI-derived NDVI against Landsat 7 ETM+ by cross-comparison and by comparing with Moderate Resolution Imaging Spectroradiometer (MODIS) and Geostationary Ocean Color Imager (GOCI)-derived NDVIs as well as in-situ NDVI measurements. Simulations of Top of Atmosphere (TOA) reflectance and surface reflectance of broadleaf trees and water were conducted for Landsat 8 OLI, Landsat 7 ETM+, and MODIS in order to evaluate the impact of band pass difference on NDVI calculation. Four consecutive pairs of Landsat 8 OLI and Landsat 7 ETM+ data over China and Korea were examined, and NDVIs derived from TOA reflectance and surface reflectance by three atmospheric correction methods were evaluated. Both simulations and comparisons showed that NDVIs derived from atmospherically-corrected surface reflectance had good consistency, while the simulation showed that the agreement varied with atmospheric characteristics. The four pairs of Landsat 8 OLI and Landsat 7 ETM+ NDVI had a mean bias error within ± 0.05 , and R^2 from 0.84 to 0.98. Vegetated land cover types were found to have better NDVI agreement than non-vegetated land cover types. Especially, Landsat 8 OLI consistently generated lower NDVI values in water area than Landsat 7 ETM+, which resulted from higher aerosol optical thickness in atmosphere. Landsat 8 OLI-derived NDVI showed better agreement with MODIS and GOCI NDVI than Landsat 7 ETM+, mainly on vegetated surfaces. Both Landsat 8 OLI and Landsat 7 ETM+ surface reflectance-derived NDVI agreed well with in-situ light emitting diode (LED) NDVI measurements at a homogeneous deciduous forest site. Landsat 8 OLI was also found to produce higher spatial variability of NDVIs than Landsat 7 ETM+ at vegetated and urban areas, but lower variability on water area. The overall good agreement between Landsat 8 OLI NDVI and Landsat 7 ETM+, MODIS and GOCI NDVIs as well as in-situ measurements ensures that it is reliable to integrate the new sensor observations with those from the multiple satellite sensors, given that the same atmospheric correction methods are applied. Furthermore, the greater NDVI contrast between vegetated areas and water areas, and the higher spatial variability of Landsat 8 OLI NDVI indicated that the new sensor has better capability in land surface process monitoring, such as land cover mapping, spatiotemporal dynamics of vegetation growth, and drought assessment.

© 2015 Elsevier Inc. All rights reserved.

1. Introduction

Vegetation indices, based on remotely-sensed spectral reflectance in the near-infrared and visible bands, have been widely used for monitoring vegetation cover and health condition, plant phenology, and

ecosystem changes (Chen, Chen, & Son, 2012; De Beurs & Henebry, 2004; Glenn, Huete, Nagler, & Nelson, 2008; Gong et al., 2012; Lambert, Drenou, Denux, Balent, & Cheret, 2013). They have been used to assess climate–terrestrial interactions such as evapotranspiration (ET), heat waves, and droughts (Black & Stephen, 2014; Gao, Wang, Cao, & Gao, 2014; Pervez, Budde, & Rowland, 2014; Rhee, Im, & Carbone, 2010), and assist land cover mapping and change detection (Bhatti & Tripathi, 2014; Im, Lu, Rhee, & Jensen, 2012a; Kleynhans et al., 2011; Liu, Wang, Tani, Matsuoka, & Matsumura, 2011; Lunetta,

* Corresponding author at: School of Urban and Environmental Engineering Ulsan National Institute of Science and Technology (UNIST) 50 UNIST-gil, Eonyang-eup, Ulsan National Ulsan, South Korea, 689-798.

E-mail address: ersgis@unist.ac.kr (J. Im).

Knight, Ediriwickrema, Lyon, & Worthy, 2006). Among many vegetation indices such as Normalized Difference Vegetation Index (NDVI), Soil Adjusted Vegetation Index (SAVI) and Enhanced Vegetation Index (EVI), NDVI has been most commonly used for vegetation-related monitoring in numerous studies (Cheret & Denux, 2011; Hielkema, Prince, & Astle, 1986; Im, Lu, Rhee, & Quackenbush, 2012b; Li, Im, & Beier, 2013; Meng, Cooke, & Rodgers, 2013; Ozdemir, 2014; Yuan, Wang, & Mitchell, 2014; Zhang et al., 2003). During the recent decades, the increasing number of satellite sensors provides great opportunity for NDVI derivation at various spatial and temporal scales, and enables the synergistic use of observations from multiple satellite sensors to better understand land processes such as ET and carbon fluxes (Hong, Hendrickx, & Borchers, 2009; Tucker et al., 2005). However, a major challenge is that differences in sensor viewing conditions, spectral band responses, instrument performances, and atmospheric conditions at the time of observation increase inconsistencies in measuring surface reflectance. This contributes to difficulties in using NDVI data derived from multiple sensors (Brown, Pinzón, Didan, Morissette, & Tucker, 2006; Van Leeuwen et al. 2006; Hadjimitsis et al., 2010). Teillet and Ren (2008) pointed out that the differences in spectral wavelength of various sensors alone can lead to as large as 10% of the NDVI differences. Such inconsistency can result in unreliable monitoring of vegetation dynamics and produce uncertainties in the estimation of secondary remotely-sensed products such as ET.

While previous studies have evaluated the agreement in surface reflectance and vegetation indices derived from multiple sensors, mainly focusing on Landsat TM/ETM+ and MODIS instruments (Feng et al., 2012; Ju, Roy, Vermote, Masek, & Kovalsky, 2012; Maier-sperger et al., 2013), this study examines the characteristics of the NDVI derived from the newly launched Landsat 8 OLI sensor. Landsat 8 satellite, the latest member of Landsat family, was launched on February 11, 2013 and the data have been publicly available since May 2013. The satellite extends the 40+ years of the Landsat program and provides the continuity of earth surface observations at high spatial resolutions and multiple spectral wavebands. It carries two sensors, the Operational Land Imager (OLI) and the Thermal Infrared Sensor (TIRS). While the continuity of spectral coverage between Landsat-8 and the predecessor Landsat ETM+ was a mission consideration, the new sensors provide significant improvements. Besides the addition of two spectral bands (one deep blue visible band at 430–450 nm and a shortwave infrared band at 1360–1390 nm) and one thermal band, the other reflective wavebands corresponding to the previous Landsat ETM+ bands have narrower wavelength (Fig. 1). In particular, the previous near-infrared

(NIR) band used in the ETM+ instrument is narrowed down to 850–880 nm similar to the MODIS NIR band to avoid water vapor absorption at 825 nm wavelength. Second, the OLI sensor employs the pushbroom technology which enables the data acquisition with much better signal-to-noise (SNR) performance and higher radiometric resolution (Roy et al., 2014). Compared to 256 gray-level images from the previous 8-bit Landsat ETM+ instrument, the new Landsat 8 OLI images have a dynamic range of 12-bits (4096 levels) (Roy et al., 2014). The narrower NIR band, higher SNR, and better radiometric resolution indicate that the new OLI sensor has the potential to be less impacted by atmospheric conditions and to be more sensitive to surface reflectance variability. Thus, it may better represent the spectral properties of vegetation and enhance the detection of temporal and spatial heterogeneity of vegetation compared to Landsat 7 ETM+ data (Ding, Zhao, Zheng, & Jiang, 2014). Moreover, Landsat 8, in conjunction with Landsat 7, currently acquires images of a same scene every 8 days, enabling more temporal repetition of earth observations from the Landsat series.

Nonetheless, the difference in the spectral bands and the instrument performances between Landsat 8 OLI and its predecessors may cause variations on the derived NDVI. Although atmospheric correction methods can be applied to eliminate the effect of solar or viewing conditions and sensor spectral responses, the atmospheric effects, especially the scattering and absorption caused by aerosols still pose correction challenges (Roy et al., 2014). Besides, atmospheric correction methods, even with the same radiative transfer algorithm but different atmospheric parameterization, can produce statistically different estimations of surface reflectance, and thus NDVI (Ju et al., 2012). Thus, it is necessary to examine the NDVIs derived from different atmospheric correction methods.

To date, only a few studies have examined the characteristics of Landsat 8 OLI-based NDVI. Ding et al. (2014) examined the temporal dynamics of spatial heterogeneity of cropland NDVI based on time-series Landsat 8 OLI imagery, but did not include the agreement analysis with Landsat 7 ETM+. Li, Jiang, and Feng (2014) compared vegetation indices from Landsat 7 ETM+ and Landsat 8 OLI imagery over Mekong River Basin and found extremely high consistency of vegetation indices ($R^2 > 0.99$). In Li et al. (2014), the Fast Line-of-sight Atmospheric Analysis of Hypercubes (FLAASH) atmospheric correction was applied to both sensor images for surface reflectance retrieval, but it was unclear how the selection of atmospheric correction methods affects the resultant consistency of vegetation indices. In the present study, we conducted a comprehensive examination of the characteristics of the Landsat 8 OLI-derived NDVI using the Landsat ETM+ as a baseline comparison

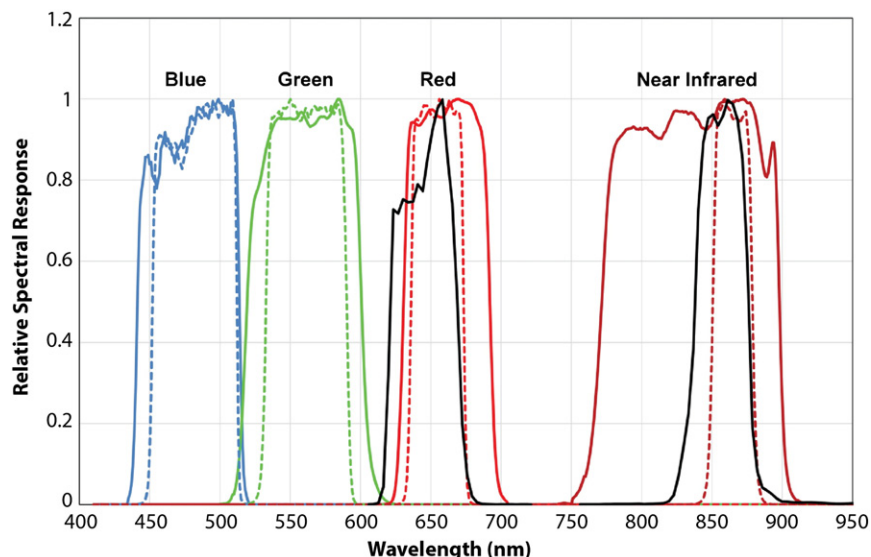


Fig. 1. Band average relative spectral response of Landsat 7 ETM+ (solid line), Landsat 8 OLI (dash line) and MODIS (black).

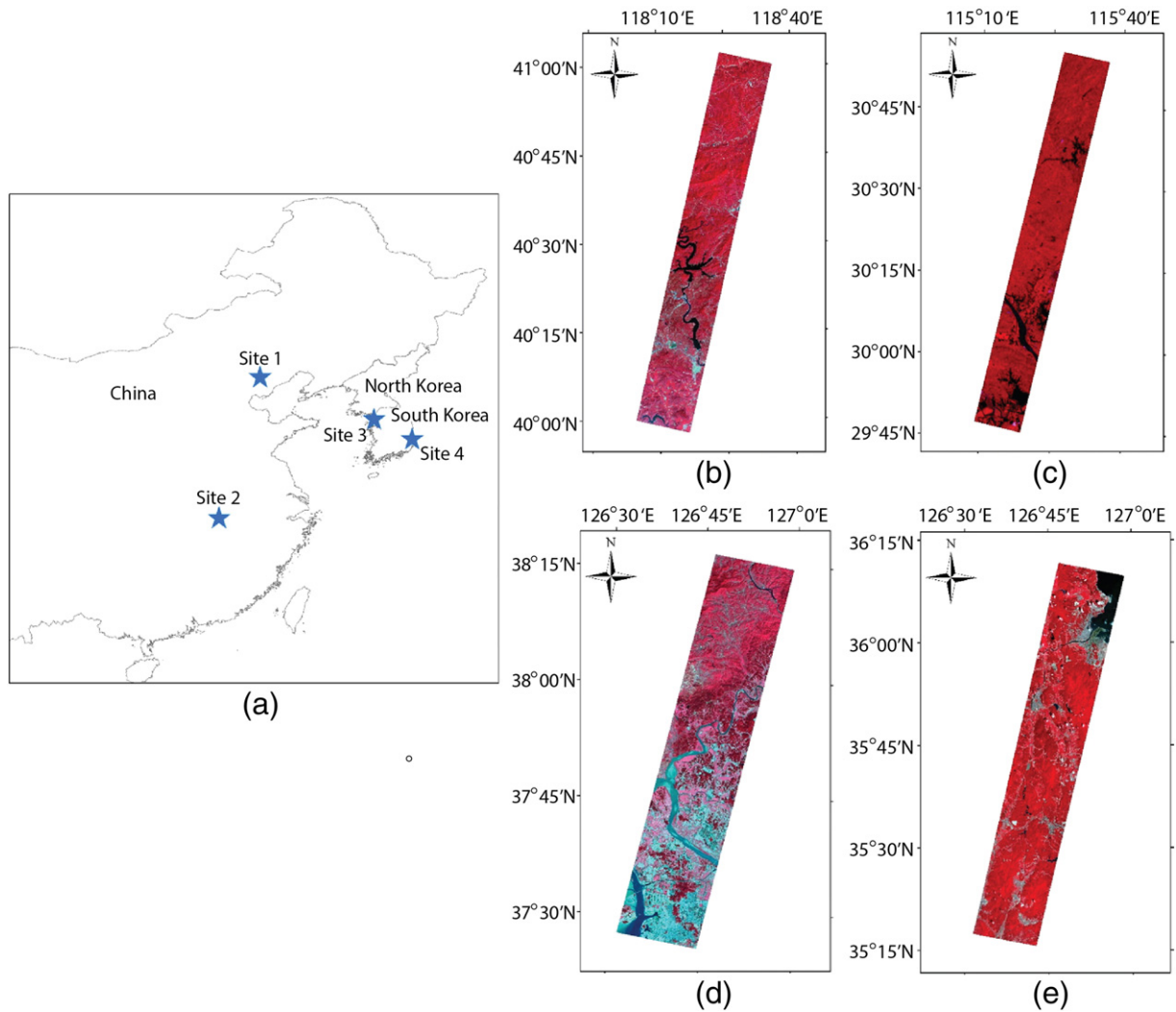


Fig. 2. (a) Location of four study sites, and Landsat 8 OLI color-infrared images showing the study sites: (b) site 1 (P122, R32); (c) site 2 (P122, R39); (d) site 3 (P116, R34); and (e) Site 4 (P114, R35).

from the following four aspects: (1) the effect of band pass differences and atmospheric condition on NDVI calculation by TOA and surface reflectance simulation for Landsat 8 OLI, Landsat 7 ETM+, and MODIS; (2) NDVI agreement between Landsat 8 OLI and the consecutive Landsat 7 ETM+ acquisition during leaf-on season with most abundant vegetation at four study sites in China and Korea; (3) the agreements of Landsat 8 OLI (Landsat 7 ETM+) NDVI with NDVI derived from MODIS instrument, Geostationary Ocean Color Imager (GOCI) data acquired on the same day, and in-situ LED measurement; and (4) the spatial variability of NDVI revealed by Landsat 8 OLI in comparison with Landsat 7 ETM+. Both Landsat 8 OLI and Landsat 7 ETM+ NDVIs at the four study sites were derived based on TOA reflectance, and surface reflectance computed from three different atmospheric correction methods including Second Simulation of a Satellite Signal in the Solar Spectrum Vector (6SV) radiative transfer algorithm, Dark Object

Subtraction (DOS), and FLAASH in the ENVI software. All comparisons were conducted over different land cover types.

2. Data and preprocessing

2.1. Landsat 8 OLI and Landsat 7 ETM+ data

Landsat 8 acquires data over the earth surface every 16 days with an 8-day offset from Landsat 7. In this study, four consecutive pairs of Landsat 8 OLI and Landsat 7 ETM+ Level 1 terrain-corrected (L1T) products over China and Korea were selected based on the following criteria: (1) images were collected during the leaf-on season with most abundant leafage (usually July to September) in order to minimize the phenological (and thus spectral) variability during the 8-day interval; (2) images had minimal cloud cover (<1%) at the scene center;

Table 1
Pairs of Landsat 8 OLI and Landsat 7 ETM+ data.

Site no.	Path/row	Acquisition date		Coordinates (lon, lat)	Area (km ²)
		Landsat 8	Landsat 7		
1	122/32	9 August 2013	17 August 2013	118.2, 40.3	2022
2	122/39	9 August 2013	17 August 2013	115.3, 30.3	2060
3	116/34	16 September 2013	8 September 2013	126.8, 37.9	1802
4	114/35	17 August 2013	9 August 2013	129.3, 35.7	1829

Table 2
Land cover reclassification.

Global land cover products			Reclassification
MCD12Q1 IGBP	GlobCover 2009	FROM-GLC (level 1)	
Evergreen Needleleaf forest	Closed to open broadleaved evergreen or semi-deciduous forest	Forest	Forest
Evergreen Broadleaf forest	Closed broadleaved deciduous forest		
Deciduous broadleaf forest	Closed needleleaved evergreen forest		
Mixed forest			
Cropland	Post-flooding or irrigated croplands (or aquatic)	Crop	Crop
Cropland/natural vegetation mosaic	Rainfed croplands		
	Mosaic cropland (50–70%)/vegetation (grassland/shrubland/forest) (20–50%)		
Urban and built-up	Artificial areas	Impervious	Urban
Water	Water bodies	Water	Water

only the sub-image at the scene center was used because of the SLC-off problem of Landsat 7 ETM+; and (3) images over the study sites included different land cover types so that the NDVI comparison by land cover type can be conducted. The selected study sites are summarized in Table 1 and located in Fig. 2. All study sites have forest, crop, urban, and water body cover types according to MODIS Land Cover Type (MCD12Q1) products during 2012.

Cloud and cloud shadow in each of Landsat 8 OLI and Landsat 7 ETM+ images were detected and the mask layers were generated using the “Fmask” algorithm (Zhu & Woodcock, 2012; <https://code.google.com/p/fmask/>). For Landsat 8 OLI images, the cloud and cloud shadow masks, in combination with Landsat 8 OLI L1T-provided Quality Assurance (QA) data were used to remove contamination by clouds or shadows.

2.2. MODIS and GOCI data

MODIS data on the same days of the Landsat 8 and 7 acquisitions were obtained as a baseline comparison. It is ideal to use MODIS Terra daily gridded surface products (MOD09GA Collection 5) because the local crossing time of MODIS Terra sensor is approximately 10:30 am, only 15–30 min past Landsat observations (10:00–10:15 am), and collect the data for both in a descending mode. In case of poor quality issues caused by MODIS calibration errors (Feng et al., 2012), MODIS Terra products collected within ±2 days were also considered as valid. If none of these products were cloud free at the study area, the MODIS Aqua surface reflectance products (MYD09GA) on the same days of Landsat 7 and 8 collection were used instead. The 500 m MOD09GA (or MYD09GA) product was re-projected with the same

projection system as Landsat 7 and 8 data. Clouds, cloud shadows, cirrus, or areas with high aerosol amounts detected in the product’s quality assurance (QA) band were removed. It should be noted that the MODIS surface reflectance product was derived based on 6SV radiative transfer model (Vermeote & Vermeulen, 1999).

Geostationary Ocean Color Imager (GOCI), the world’s first geostationary satellite sensor for monitoring ocean color, provides 8 images per day from 9:00 am to 4:00 pm with an hour interval at 8 bands with 500 m spatial resolution covering Korea, Japan, and parts of China, Mongolia, and Russia (Yeom & Kim, 2013). GOCI data are collected approximately 30 min after each hour over the study sites in Korea. GOCI data collected at 10:30 am on the same day of the Landsat 8 and 7 acquisitions were used for comparison. Surface reflectance for each scene was derived using MODIS-based 6S radiative transfer model (Section 2.5.1). GOCI bands 5 (650–670 nm) and 8 (845–885 nm) were used to calculate NDVI similar to the MODIS bands used for NDVI calculation. While GOCI data have been mainly used for ocean water applications, they have proved useful for land applications as well (Yeom & Kim, 2013).

2.3. Ground reflectance by LED

To evaluate Landsat NDVI, we used in-situ NDVI data using light emitting diode (LED)-sensors at the Gwangneung Experimental Forest in South Korea. The sensors were installed at the top of two towers located in a deciduous broadleaf forest (latitude: 37.748717°N, longitude: 127.148176°E, elevation: 260 m, slope: 10–20°) and an evergreen needleleaf forest (latitude: 37.74843°N, longitude: 127.162593°E, elevation: 128 m, slope: <3°). The deciduous forest is dominated by *Quercus acutissima*, *Quercus serrate* and *Carpinus laxiflora* and the peak LAI was around 4 (Ryu, Lee, Jeon, Song, & Kimm, 2014). The semivariogram analysis revealed the scale of heterogeneity, defined as “range”, in this site was ~1 km (Ryu, Kang, Moon, & Kim, 2008). The evergreen site is an artificially planted and managed forest with a single dominant species, *Abies holophylla* and the peak LAI was 8.3. The homogeneous evergreen forest that is surrounded by deciduous forest, resulted in 50% coverage of deciduous forest within a 500 m pixel centered on the evergreen forest tower (Ryu et al., 2014). LED-sensors measured bi-hemispheric spectral reflectance of red, green, blue and NIR bands. Here, we used red (peak: 646 nm, Full Width at Half Maximum (FWHM): 56 nm) and NIR (peak: 843 nm, FWHM: 72 nm)

Table 3
Geometry and atmosphere parameters used in MODTRAN.

Date	Solar zenith angle (°)	Water vapor content (g/cm ²)	Aerosol optical thickness (km)	AOT corresponding visibility (km)
9 August 2013	32.94	0.1	0.16	50
		0.5	0.19	40
		1.0	0.25	30
		2.0	0.4	20
		3.0	0.65	10

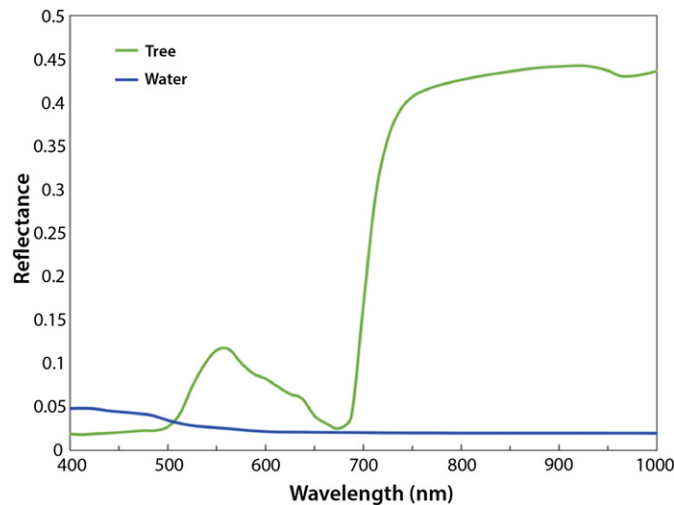


Fig. 3. Surface reflectance curve of green broadleaf trees (green) and water (blue) used to simulate TOA radiance.

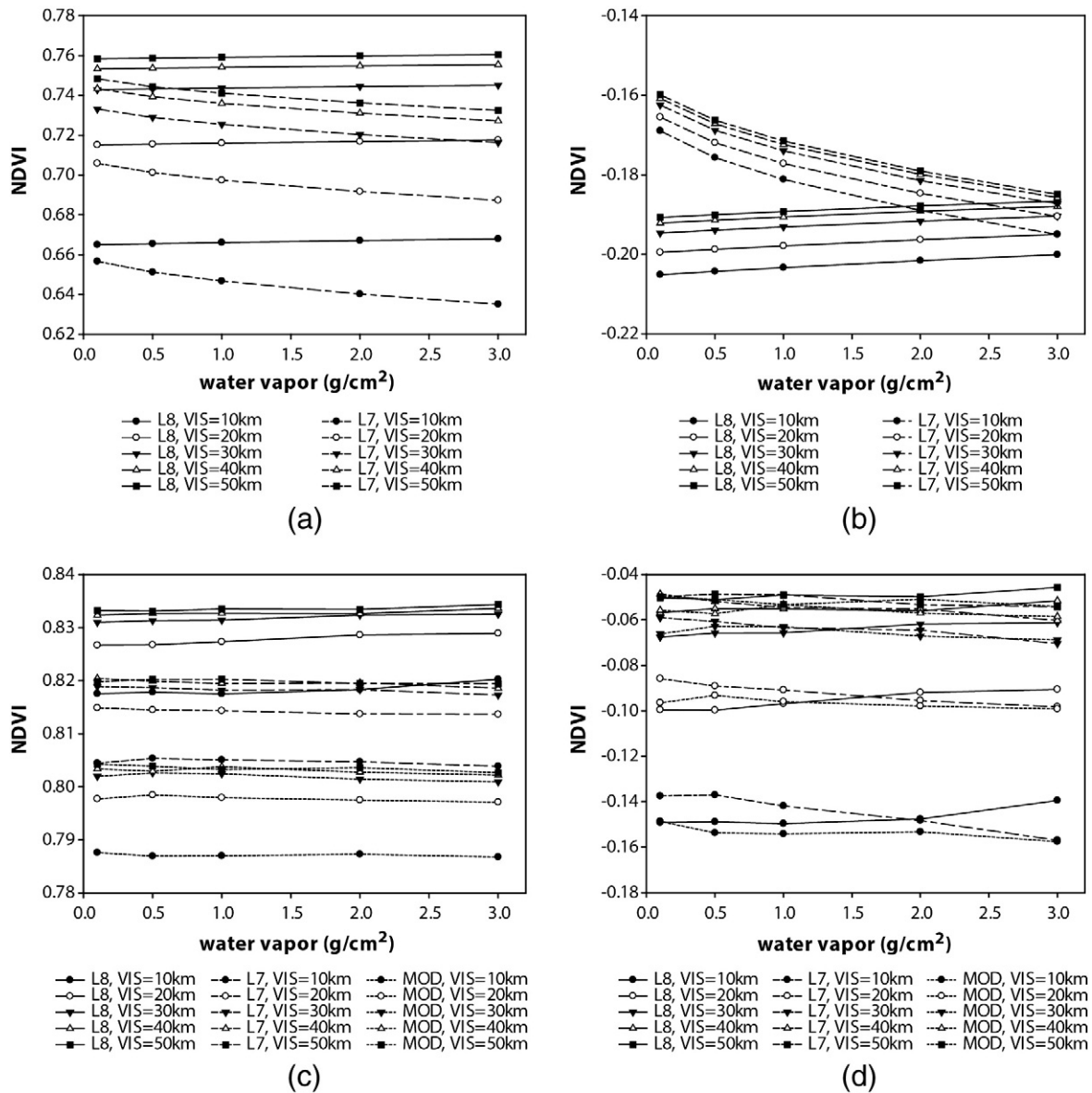


Fig. 4. NDVI derived from simulated reflectance of Landsat 8 OLI (solid line), Landsat 7 ETM+ (dash-dotted line), and MODIS Terra (dotted line) instruments for tree and water on 9 August 2013. (a) Tree NDVI derived from MODTRAN-simulated TOA reflectance; (b) water NDVI derived from MODTRAN-simulated TOA reflectance; (c) tree NDVI from MOTRAN-6SV simulated surface reflectance; (d) water NDVI from MOTRAN-6SV simulated surface reflectance.

bi-hemispheric reflectance data to compute for NDVI. Data were collected every second and stored as half-hourly mean values. Development and evaluation of LED-sensors were reported in [Ryu et al. \(2010\)](#), and detailed descriptions on the LED-sensor settings in the Gwangneung forest appear in [Ryu et al. \(2014\)](#).

2.4. Land cover map

Three land cover products: MODIS Global 500 m Terra and Aqua combined the yearly gridded land cover product (MCD12Q1 IGBP) from NASA (https://lpdaac.usgs.gov/products/modis_products_table/mcd12q1), European Space Agency (ESA) Global Land Cover Map 2009 products (also called GlobCover 2009) with 300 m resolution, and the Finer Resolution Observation and Monitoring of Global Land Cover (FROM-GLC) with 30 m resolution developed by Tsinghua University, China ([Gong et al., 2013](#)) were downloaded, re-projected to the same projection system as Landsat 7 and 8 data, and combined to create a new ensemble 30 m land cover map in the study sites to ensure the most accurate land cover classification. Due to the differences

in the classification schemes used in these products, each land cover product was simply reclassified to forest, crop, urban, and water body classes based on the criteria listed in [Table 2](#). To minimize uncertainties in each land cover product, only the overlapping patches with the same class from all three reclassified maps and with area over 0.25 km² were used to produce the new land cover map, which was used as reference land cover data for subsequent NDVI analyses.

2.5. Atmospheric correction for Landsat 7 ETM+ and 8 OLI data

Each Landsat 7 and 8 L1T Digital Number (DN) image was converted to TOA reflectance based on the available Landsat 8 OLI and Landsat 7 ETM+ calibration coefficients and standard correction formulas (http://landsat.usgs.gov/Landsat8_Using_Product.php; [Chander, Markham, & Helder, 2009](#)). Although the Disturbance Adaptive Processing System (LEDAPS) surface reflectance product provided from the U.S. Geological Survey (USGS) Earth Resources Observation and Science (EROS) Center was available for Landsat 7 ETM+, to be consistent, both Landsat 7 ETM+ and Landsat 8 OLI images were processed using

the same atmospheric correction methods including MODIS-based 6SV, Dark Object Subtraction (DOS), and FLAASH models.

2.5.1. 6SV atmospheric correction

Ju et al. (2012) presented a MODIS-based 6SV atmospheric correction method for Landsat 7 ETM+ data. Both MODIS-based and LEDAPS methods are based on the 6SV radiative transfer model, but differ in the atmospheric parameterization approaches, with the biggest difference in Aerosol Optical Thickness (AOT) characterization. The MODIS-based method uses MODIS Terra-derived AOT, while the LEDAPS algorithm derives AOT independently from each Landsat 7 ETM+ image using a dense dark vegetation (DDV) approach. Using AERONET in-situ measurements as reference, the MODIS-based method was reported to have better performance than the LEDAPS method. The latter tended to overestimate surface reflectance (Ju et al., 2012). Our study adopted a similar approach as the MODIS-based method to build an atmospheric correction model for both Landsat 7 ETM+ and Landsat 8 OLI data. The MODIS aerosol product (MOD04L2 Collection 5.1) and the water vapor product (MOD05L2 Collection 5.1) were downloaded for each study area on the dates of the Landsat data acquisition. Ozone data from the NASA Earth Probe Total Ozone Mapping Spectrometer (EP TOMS) (Masek et al., 2006) and elevation data from Shuttle Radar Topography Mission (SRTM) 90 m global Digital Elevation Model (DEM) product were used for the 6SV implementation. The aerosol optical depth at 550 nm from MOD04L2, water vapor at near-infrared band from MOD05L2, ozone, and SRTM DEM were all interpolated to 0.05° grid. Using these parameters, with assumption of the continental aerosol type and mid-latitude summer aerosol model, a look-up table of the atmosphere coefficients was built and the surface reflectance values were then estimated from each of the Landsat TOA reflectance values.

2.5.2. DOS atmospheric correction method

The dark object subtraction method (Chavez, 1988) was applied to both Landsat 8 OLI and Landsat 7 ETM+ images. In Landsat 8 OLI data, dark objects were first established as pixels with the “lowest valid value” in visible bands. The “lowest valid” DN value was determined as the one that has an interval of ≤ 100 with its near neighbor in the low end of the histogram. For example, if three lowest DN values in the histogram are 4028, 5159, and 5231 respectively, the DN of 5159 was identified as “lowest valid value” as the lowest DN 4028 was deemed as noise. The haze radiance in the near infrared bands were then found from the continuous relative scatter lookup table established following Chavez’ (1988) method that assumes a power relationship between band haze radiance (GIS Ag Maps, 2014). Haze radiance in Landsat 7 ETM+ images were calculated in similar way as in Landsat 8 OLI images (GIS Ag Maps, 2014).

2.5.3. FLAASH atmospheric correction method

The FLAASH atmospheric correction model embedded in the ENVI software was applied for both Landsat 7 ETM+ and Landsat 8 OLI images. The FLAASH method was developed based on the MODTRAN radiation transfer code. Uniform parameters were specified for both types of images: the mid-latitude summer atmospheric model, the rural aerosol model, and the 2-Band aerosol retrieval method.

3. Methods

3.1. NDVI simulation and comparison

To evaluate the impact of band pass difference on NDVI calculation, TOA radiance was simulated for red/NIR bands of Landsat 8 OLI, Landsat 7 ETM+, and MODIS Terra based on USGS spectral surface reflectance of broadleaf trees and water (Fig. 3) using MODTRAN. 6SV radiative transfer code was then used to derive simulated surface reflectance from TOA radiance. The ground pixel was assumed to be located at the center of

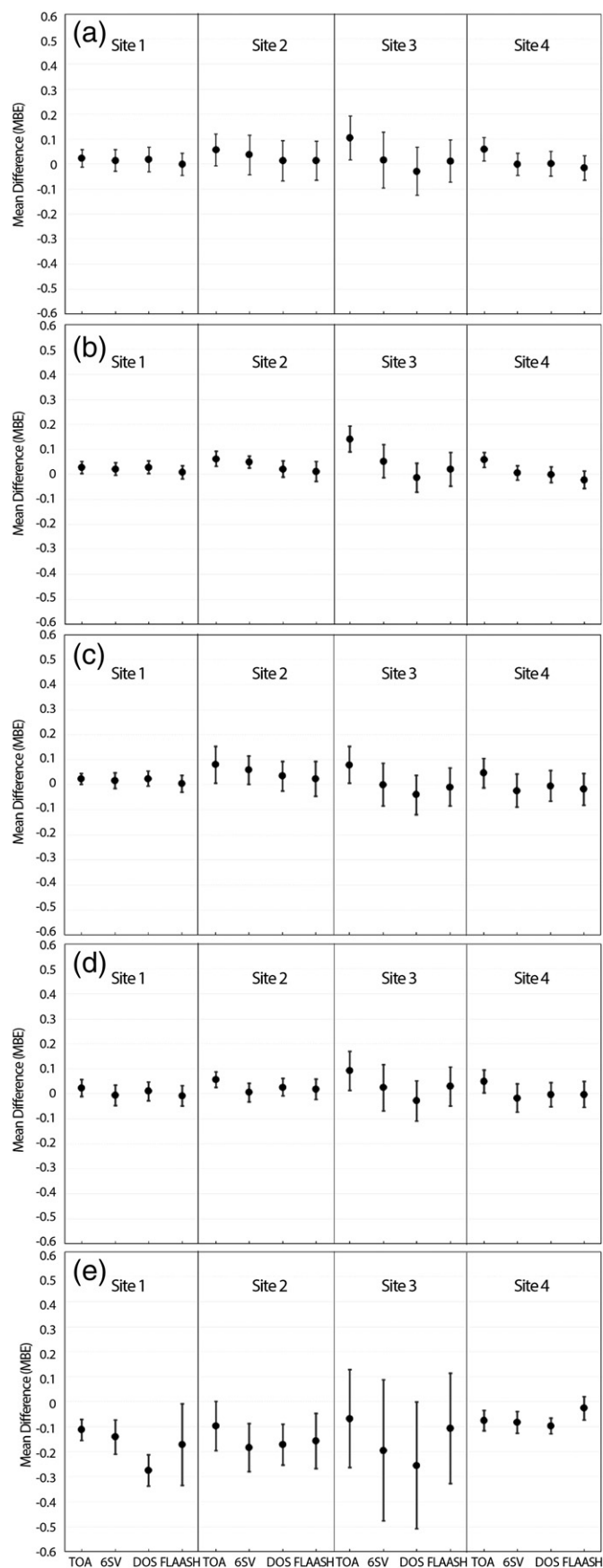


Fig. 5. Mean differences (MBE) derived from Landsat 8 OLI and Landsat 7 ETM+ at the four study sites, with error bars showing the standard deviation (SDBE). (a) Overall; (b) forest; (c) crop; (d) urban; (e) water.

Table 4
Comparison between Landsat 8 OLI NDVI and Landsat 7 ETM+ NDVI derived from TOA reflectance and surface reflectance from three atmospheric correction methods.

	Site 1					Site 2					Site 3					Site 4					
	N	R ²	RMSD	a	b	n	R ²	RMSD	a	b	n	R ²	RMSD	a	b	n	R ²	RMSD	a	b	
<i>Overall</i>																					
TOA	220,924	0.980	0.040	1.126	−0.064	487,243	0.967	0.086	1.153	−0.025	141,261	0.903	0.132	1.172	0.029	629,412	0.896	0.068	1.064	0.013	
6SV		0.972	0.043	1.167	−0.116		0.950	0.094	1.207	−0.085		0.890	0.113	1.146	−0.058		0.918	0.045	1.123	−0.100	
DOS		0.964	0.061	1.311	−0.216		0.947	0.085	1.174	−0.093		0.891	0.107	1.140	−0.116		0.845	0.049	1.095	−0.036	
FLAASH		0.970	0.042	1.173	−0.136		0.937	0.084	1.098	−0.052		0.913	0.089	1.029	−0.008		0.908	0.049	0.976	−0.002	
<i>Forest</i>																					
TOA	198,596	0.902	0.034	0.969	0.050	69,655	0.687	0.069	0.773	0.210	44,603	0.629	0.151	1.124	0.071	460,422	0.788	0.065	0.877	0.143	
6SV		0.879	0.032	1.025	0.001		0.798	0.054	0.923	0.108		0.641	0.084	1.088	−0.014		0.808	0.043	1.002	0.005	
DOS		0.894	0.036	1.007	0.023		0.634	0.038	0.735	0.229		0.674	0.058	1.060	−0.061		0.774	0.031	0.914	0.071	
FLAASH		0.884	0.025	1.025	−0.012		0.641	0.040	0.716	0.245		0.664	0.065	0.854	0.134		0.756	0.042	0.848	0.108	
<i>Crop</i>																					
TOA	14,365	0.936	0.036	1.006	0.019	377,338	0.785	0.085	0.890	0.128	47,082	0.828	0.108	1.208	−0.022	167,440	0.892	0.075	1.153	−0.039	
6SV		0.938	0.035	1.058	−0.029		0.803	0.081	0.953	0.088		0.819	0.086	1.208	−0.125		0.897	0.070	1.130	−0.113	
DOS		0.937	0.037	1.030	0.001		0.769	0.066	0.870	0.119		0.825	0.089	1.214	−0.179		0.895	0.062	1.141	−0.100	
FLAASH		0.935	0.032	1.036	−0.024		0.775	0.071	0.827	0.140		0.835	0.075	1.015	−0.019		0.899	0.066	1.024	−0.034	
<i>Urban</i>																					
TOA	1082	0.825	0.041	0.993	0.024	626	0.871	0.065	1.151	0.034	43,238	0.684	0.120	1.397	0.026	1361	0.853	0.067	1.103	0.026	
6SV		0.824	0.041	1.047	−0.016		0.853	0.037	1.119	−0.023		0.667	0.096	1.371	−0.066		0.813	0.059	1.003	−0.019	
DOS		0.822	0.038	1.009	0.008		0.847	0.043	1.104	0.000		0.686	0.085	1.339	−0.137		0.845	0.049	1.095	−0.036	
FLAASH		0.823	0.041	0.985	−0.005		0.841	0.045	1.042	0.009		0.737	0.083	1.190	−0.021		0.858	0.052	0.963	0.009	
<i>Water</i>																					
TOA	6881	0.397	0.120	0.607	−0.154	39,624	0.491	0.112	0.554	−0.202	6338	0.578	0.208	1.758	−0.024	189	0.565	0.086	1.230	−0.063	
6SV		0.217	0.157	0.349	−0.088		0.471	0.207	0.563	−0.247		0.620	0.343	1.987	−0.174		0.460	0.093	0.449	−0.019	
DOS		0.231	0.282	0.621	−0.250		0.749	0.190	0.588	−0.201		0.574	0.359	2.024	−0.363		0.204	0.102	0.497	0.008	
FLAASH		0.167	0.187	0.260	−0.120		0.334	0.191	0.340	−0.279		0.590	0.245	1.484	−0.090		0.241	0.053	0.396	−0.003	

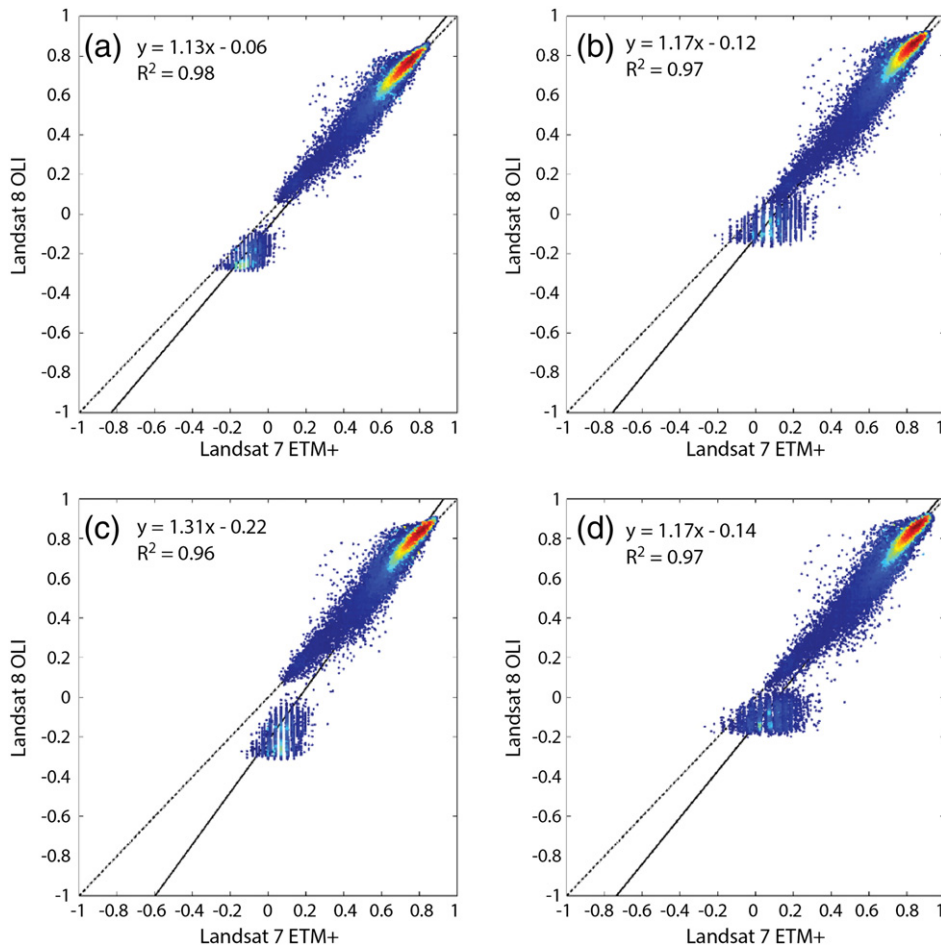


Fig. 6. Scatter plots of Landsat 8 OLI NDVI versus Landsat 7 ETM + NDVI at site 1 based on reflectance derived from (a) TOA radiance; (b) 6SV atmospheric correction; (c) DOS atmospheric correction and (d) FLAASH atmospheric correction methods. The solid lines show linear regression model fits of the NDVIs. The dashed lines are 1:1 lines for reference. The color of the points illustrate the frequency of the NDVI values (red most frequent, blue least frequent).

site 1 (40.3°N, 118.3°E), and the Landsat/MODIS data was assumed to be acquired at 10:30 am on 9 August 2013, the same date and time as the Landsat 8 OLI data collection at site 1. Although the actual Landsat 8 OLI and Landsat 7 ETM + acquisition is 8-day apart, the solar geometry does not vary significantly at the same time of the day. The mid-latitude summer atmosphere model and rural aerosol model were used to represent atmospheric condition in MODTRAN. Atmospheric multiple scattering was simulated using the 8-stream DISORT algorithm with azimuthal dependence. Since the amount of water vapor and aerosol content can vary day by day and can significantly affect TOA radiance, different water vapor and aerosol properties were customized as shown in Table 3. Water vapor content ranged from 0.1 to 3.0 which were typical in mid-latitude summer atmosphere. Aerosol optical thickness values were set from 0.16 to 0.4, with corresponding visibility distance from 50 km to 10 km. A total of 25 combinations of the parameters were used to simulate TOA radiance in MODTRAN.

TOA radiance simulated by MODTRAN was used to calculate TOA reflectance at red and NIR bands for Landsat 8 OLI and Landsat 7 ETM +, and then TOA NDVI was calculated and compared. The 6S radiative transfer code with the same combinations of atmospheric and geometric parameters was used calculate surface reflectance for Landsat 8 OLI, Landsat 7 ETM +, and MODIS, NDVI was then calculated for comparison.

3.2. NDVI generation from Landsat, MODIS and GOCI sensor

For each of the Landsat 8 OLI and Landsat 7 ETM + images in the four study sites, four sets of 30 m NDVI (Eq. 1) were calculated based on red

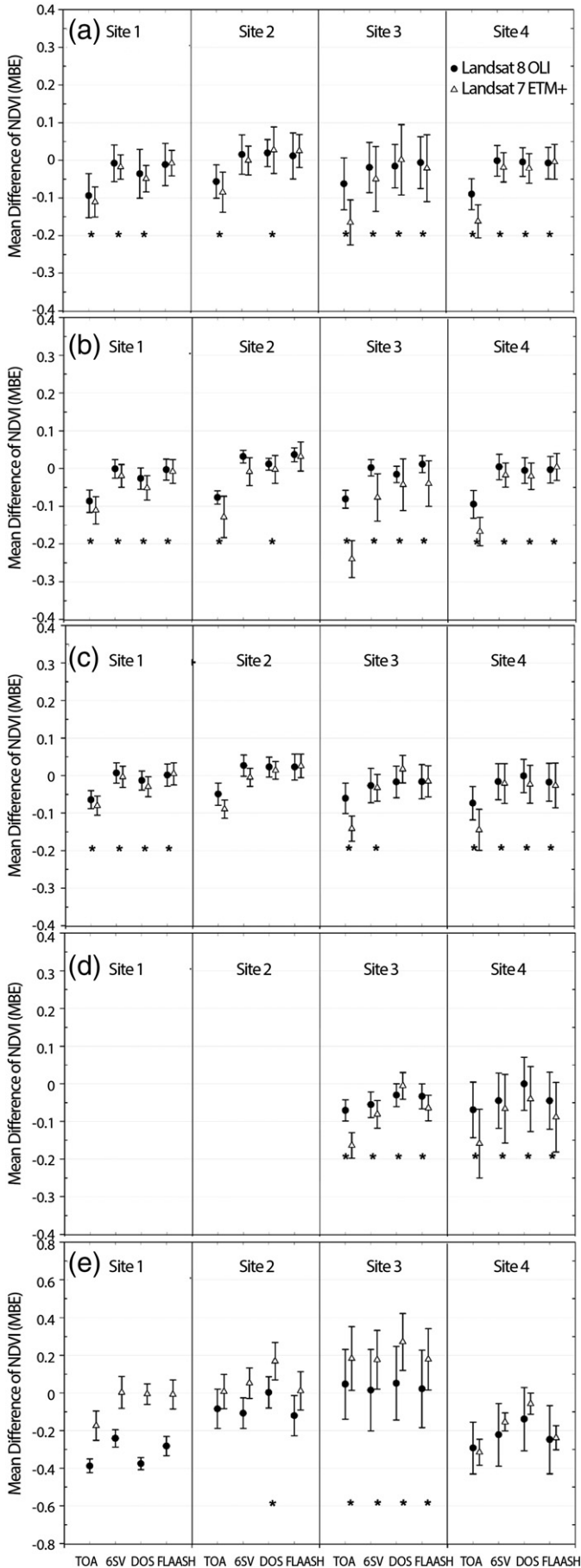
and near-infrared TOA reflectance, surface reflectance derived from the MODIS-based 6SV model, DOS, and FLAASH methods. NDVIs at a resolution of 500 m were also calculated from MODIS MOD09GA surface reflectance products and GOCI-derived surface reflectance. Landsat cloud, cloud shadow, and cirrus masks and MODIS QA masks were used to remove pixels with low quality so that only NDVI values from good-quality reflectance retrieval were evaluated. Since GOCI does not provide cloud, cloud shadow, and cirrus masks, visual inspection was applied to identify pixels with low quality for removal.

$$\text{NDVI} = \frac{\rho_{\text{nir}} - \rho_{\text{red}}}{\rho_{\text{nir}} + \rho_{\text{red}}} \quad (1)$$

where ρ_{red} and ρ_{nir} are TOA or surface reflectance at red and near-infrared band, respectively.

3.3. NDVI comparisons between Landsat 8 OLI and Landsat ETM +

For each study site, the NDVI agreements between Landsat 8 OLI and Landsat 7 ETM + were measured based on (1) TOA reflectance-derived NDVI; (2) 6SV-derived NDVI; (3) DOS-derived NDVI; and (4) FLAASH-derived NDVI. The reclassified land cover maps were used to locate NDVI pixels with forest, crop, urban, or water land cover types. For each of and all land cover types, a simple linear regression model (Eq. 2) was built to examine the relationship between Landsat 8 and 7 NDVI. The R^2 and Root Mean Square Differences (RMSD) were used to evaluate the model goodness-of-fit. Consistency metrics such as Mean



Bias Error (MBE) (Eq. 3) and the standard deviation of the bias error (SDBE) were calculated to assess the agreement between Landsat 8 and 7 NDVIs.

$$NDVI_{L8} = a \times NDVI_{L7} + b \quad (2)$$

$$MBE = \sum_{i=1}^n \frac{NDVI_{L8}(i) - NDVI_{L7}(i)}{n} \quad (3)$$

where $NDVI_{L8}$ and $NDVI_{L7}$ are NDVI derived from Landsat 8 OLI and Landsat 7 ETM +, respectively; a represents the linear slope and b is the linear model intercept; and n represents the number of NDVI pixels.

3.4. Comparisons of Landsat NDVI with MODIS, GOCI and LED

Because of the coarser resolution of MODIS and GOCI, Landsat 30 m NDVIs with pixel centroid within each MODIS 500 m grid were averaged to generate Landsat 500 m NDVI. The 500 m land cover map was also produced with majority (>75%) of land cover type within each 500 m MODIS pixel. For each study area and land cover type, Landsat 8 OLI and Landsat 7 ETM + NDVI derived from each of the above TOA or surface reflectance were compared with the same day MODIS and GOCI NDVIs. Agreement analysis was conducted with the same metrics stated in the above section. Statistical analysis was performed with the null hypothesis of mean absolute differences between Landsat 8 OLI and MODIS/GOCI NDVI greater than or equal that between Landsat 7 ETM + and MODIS/GOCI NDVI. Rejection of the null hypothesis means that the Landsat 8 OLI NDVI is statistically closer to MODIS/GOCI NDVI than Landsat 7 ETM +.

LED-NDVI data are generated from a LED-sensor mounted at the top of towers which were 3–10 m higher than top of canopies. Thus, LED-NDVI data are almost free from atmospheric contaminations such as clouds, haze, and aerosols. We selected the half-hour LED-NDVI data which was closest to the Landsat overpass time. Landsat, MODIS, and GOCI NDVI were computed within the single pixel containing the site location and compared with LED-NDVI data.

3.5. Spatial variability analysis

The NDVI spatial variability was analyzed at various spatial scales. Both Landsat 8 OLI and Landsat 7 ETM + NDVI pixels with 30 m resolution were aggregated to bigger grids with 90 m, 150 m, 300 m, and 500 m cell sizes, and the standard deviation of the NDVI values within each grid was calculated. The mean standard deviation (MSD) across the study sites and each land cover type (Eq. 4) was used to represent the average spatial variability and comparisons between Landsat 8 OLI and Landsat 7 ETM + MSD were performed.

$$MSD = \frac{1}{N} \sum_{i=1}^N \sqrt{\frac{1}{n} \sum_{k=1}^n (NDVI(k) - \overline{NDVI})^2} \quad (4)$$

where $NDVI(k)$ is the NDVI in the k th pixel in the bigger grid cell with a total of n 30 m pixels inside. \overline{NDVI} is the mean NDVI within the grid cell, and N is the total number of bigger grid cells.

Fig. 7. The mean NDVI differences between Landsat 8 OLI/Landsat 7 ETM + and MODIS. The error bars show the standard deviation of the differences. (a) Overall; (b) forest; (c) crop; (d) urban; (e) water. No information was given due to few urban samples for sites 1 and 2 in (d). * denotes that the absolute differences between Landsat 8 OLI and MODIS NDVI are significantly smaller than that between Landsat 7 ETM + and MODIS NDVI.

Table 5
Comparisons between Landsat NDVI derived from TOA or atmospherically corrected surface reflectance and the same-day MODIS NDVI for the study sites 1–4.

	Site 1										Site 2									
	Landsat 8 OLI vs. MODIS					Landsat 7 ETM+ vs. MODIS					Landsat 8 OLI vs. MODIS					Landsat 7 ETM+ vs. MODIS				
	n	R ²	a	b	RMSD	R ²	a	b	RMSD	n	R ²	a	b	RMSD	R ²	a	b	RMSD		
TOA	665	0.947	1.360	-0.386	0.111	0.931	1.039	-0.142	0.118	1887	0.977	1.002	-0.058	0.072	0.977	0.865	-0.009	0.100		
6S		0.958	1.289	-0.242	0.049	0.947	0.945	0.027	0.037		0.983	1.124	-0.059	0.055	0.981	0.929	0.040	0.039		
DOS		0.951	1.423	-0.378	0.074	0.936	0.918	0.018	0.060		0.985	1.001	0.019	0.041	0.973	0.830	0.123	0.068		
FLAASH		0.957	1.349	-0.293	0.057	0.944	0.975	0.013	0.035		0.974	1.131	-0.067	0.062	0.974	1.011	0.019	0.050		
	Site 3										Site 4									
	Landsat 8 OLI vs. MODIS					Landsat 7 ETM+ vs. MODIS					Landsat 8 OLI vs. MODIS					Landsat 7 ETM+ vs. MODIS				
	n	R ²	a	b	RMSD	R ²	a	b	RMSD	n	R ²	a	b	RMSD	R ²	a	b	RMSD		
TOA	654	0.969	0.963	-0.054	0.083	0.893	0.955	-0.144	0.175	2287	0.851	0.889	-0.002	0.099	0.821	0.854	-0.043	0.168		
6S		0.948	1.022	-0.031	0.069	0.910	0.832	0.047	0.100		0.887	1.062	-0.051	0.041	0.871	0.985	-0.006	0.043		
DOS		0.919	0.853	0.063	0.081	0.896	0.764	0.139	0.093		0.875	0.942	0.042	0.038	0.862	0.946	0.023	0.045		
FLAASH		0.925	0.882	0.055	0.089	0.924	0.924	0.065	0.091		0.876	1.056	-0.051	0.043	0.864	1.108	-0.092	0.047		

4. Results and discussions

4.1. Comparison of simulated NDVI

At the same solar geometry and meteorological visibility, i.e., the same level of aerosols, Landsat 8 OLI produced slightly higher TOA NDVI for trees and lower NDVI for water (Fig. 4a, b). For both tree and water, Landsat 8 OLI NDVI barely changes with varying water vapor, while Landsat 7 ETM+ NDVI slightly decreased with increasing water vapor content. The lower water NDVI, the higher tree NDVI, and unvaried NDVI with water vapor from Landsat 8 OLI sensor simulation can be explained by the TOA radiance of narrower NIR band being less influenced by water vapor absorption. Compared to water vapor content, atmosphere aerosol optical thickness is a major factor affecting TOA NDVI. High level of aerosol content corresponds to lower NDVI values. Both tree and water NDVIs derived from the simulated TOA reflectance of Landsat 8 OLI and Landsat 7 ETM+ sensors decreased with decreasing meteorological visibility, i.e., increasing aerosol optical depth: from 0.76 to 0.64 for tree NDVI and -0.18 to -0.21 for water NDVI (Fig. 4a, b).

After 6SV correction on TOA radiance at the same solar zenith angle, all three sensors produced stable tree NDVI with varying water vapor. Although Landsat 8 OLI produced slightly higher tree NDVI than the other instruments, the differences were minimal, within 0.03 at the same aerosol level. Aerosol optical thickness affects water NDVI more than tree NDVI. When meteorological visibility decreases from 50 km to 10 km, NDVI values dropped from above -0.05 to around -0.15. At the same level of aerosol optical thickness, all three sensors produced similar water NDVI despite of atmosphere water vapor. Comparison of Fig. 4b and 4d demonstrated that water NDVI from surface reflectance was more sensitive to atmospheric condition than tree NDVI. After 6SV correction, water NDVI varied from -0.05 to -0.16. Because NIR and red reflectance are both low for water, small change in the reflectance measurement may produce great differences in NDVI.

When Terra MODIS imagery was not available due to its low quality, Aqua MODIS data were used instead. It is found from NDVI simulations using different solar zenith angles that small changes in the angles did not influence the NDVI results much (not shown). However, it should be noted that BRDF differences between the two sensors caused by different azimuth angles and rugged terrains could be considerable.

4.2. Comparisons with Landsat 7 ETM+ NDVI

A total of 220,924, 487,243, 141,261 and 629,412 30 m pixels with good quality (not covered by cloud and cloud shadow or high aerosol) in both Landsat 7/8 and MODIS data were extracted from the four

study sites by land cover type determined based on the three land cover products, respectively. The average differences (i.e., MBE) between Landsat 8 OLI-derived and Landsat 7 ETM+-derived NDVI were within ±0.1 at all study sites and the standard deviation of the differences (i.e., SDBE) were within also 0.1 (Fig. 5a). Compared to TOA reflectance-derived NDVI, the atmospherically corrected NDVIs between Landsat 8 OLI and Landsat 7 ETM+ had better agreement, with MBE within ±0.05. Landsat 8 OLI NDVI shows strong linear relationship with Landsat 7 ETM+ NDVI at all study sites, with R² ranging from 0.84 to 0.98, and the expected deviation measured by RMSD were within 0.1, with the exception of TOA NDVI regression at site 3 (Table 4). All linear models were statistically significant at the confidence level of 95%. Although the R² values of the TOA reflectance-derived NDVI regression models were similar or even slightly higher than those derived from atmospherically-corrected reflectance, for all study sites and non-water land cover types, the biases of TOA reflectance-derived NDVI were greater than those derived from atmospherically-corrected reflectance (Fig. 5a–d). For example, at site 3 the TOA NDVI mean difference between Landsat 8 OLI and Landsat 7 ETM+ was around 0.1, while the differences decreased to 0.03 and below when atmospheric correction was applied. Examination of the images over site 3 reveals that large amount of haze and water vapor content exists on the date of Landsat 7 ETM+ image acquisition. This reduced the at-sensor radiance measured by the instrument and thus produced lower NDVI. This indicates that atmospheric correction is needed for both Landsat datasets in applications using NDVI. This atmospheric condition also explained the greater dispersion of NDVI bias error in any land cover types and the whole area (Fig. 5a–e). The scatter plots between Landsat 8 OLI and Landsat 7 ETM+ NDVI are shown in Fig. 6 with site 1 as an example. It is evident that Landsat 8 OLI and Landsat 7 ETM+ NDVI agree better at positive and higher NDVIs (i.e., Landsat 8 OLI NDVI > 0.1), while less comparable at low NDVI values typically in water area (i.e., Landsat 8 OLI NDVI < 0.1).

The mean bias of both vegetated (i.e., forest and crop) and urban NDVI derived from surface reflectance by three atmospheric correction methods were all smaller than ±0.06, while the bias of forest NDVI has a smaller variation than crop and urban NDVIs at all study sites (Fig. 5b, c). Nonetheless, crop and urban NDVIs derived from surface reflectance of Landsat 8 OLI images and that from Landsat 7 ETM+ reflectance show stronger correlation than forest NDVI, with over 75% of Landsat 7 ETM+ NDVI explained by Landsat 8 OLI NDVI at all study sites. The slope of the regression close to one and the intercept close to zero indicate a 1:1 relationship between Landsat 8 OLI and Landsat 7 ETM+ NDVI. This can be explained by the evidence that crop and urban areas generally show higher dynamic range of NDVI. It is also likely that Landsat 8 OLI has a greater capability of capturing small NDVI variance due to its higher SNR and wider radiometric range.

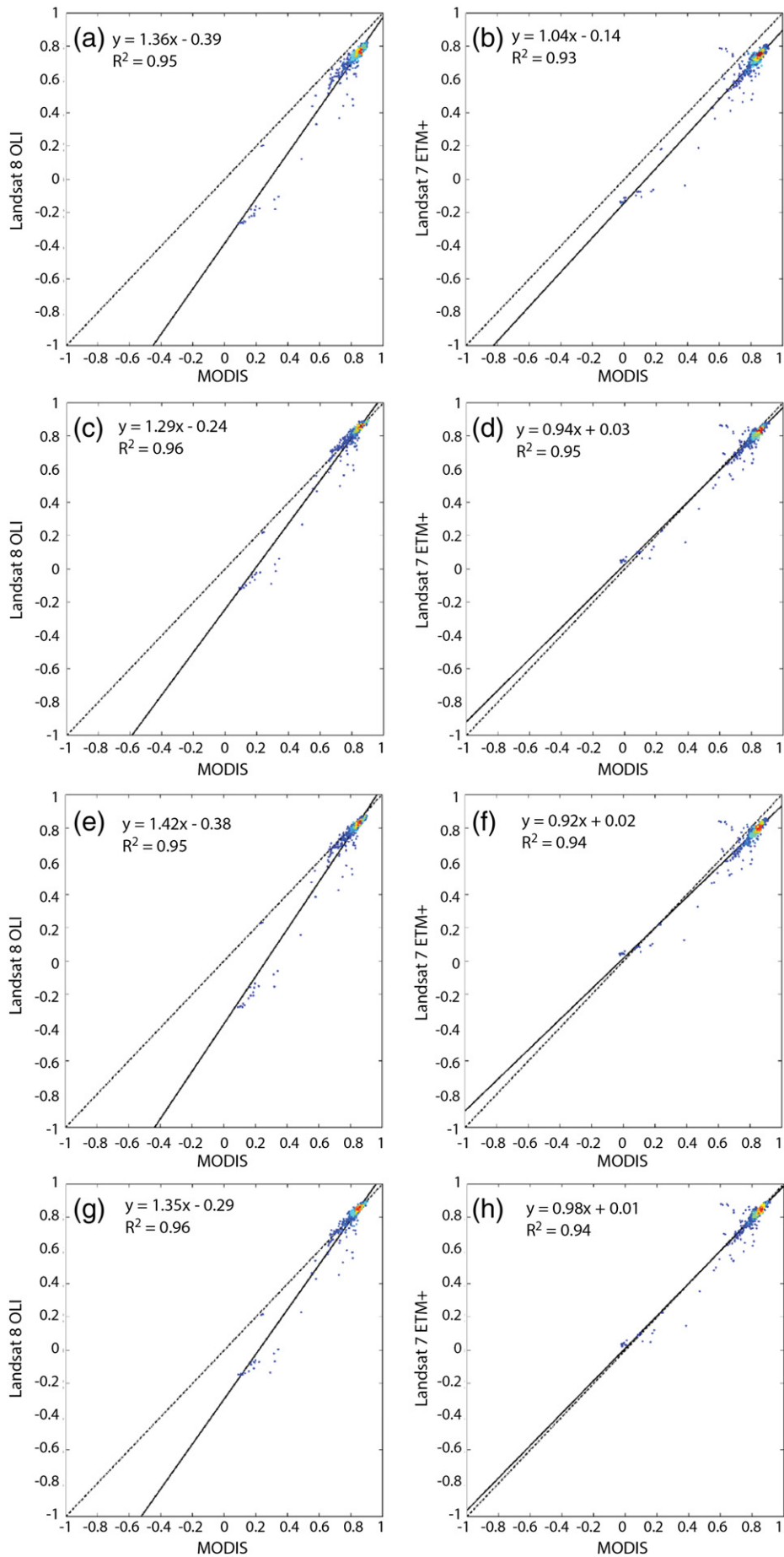


Table 6
Comparisons between Landsat NDVI derived from TOA or surface reflectance and the same-day 6S corrected GOCI NDVI.

	Site 1										Site 2									
	Landsat 8 OLI vs. GOCI					Landsat 7 ETM+ vs. GOCI					Landsat 8 OLI vs. GOCI					Landsat 7 ETM+ vs. GOCI				
	n	R ²	a	b	RMSD	R ²	a	b	RMSD	n	R ²	a	b	RMSD	R ²	a	b	RMSD		
TOA	665	0.861	1.814	-0.691	0.113	0.851	1.541	-0.461	0.094	-	-	-	-	-	-	-	-	-		
6S		0.869	1.712	-0.526	0.090	0.869	1.406	-0.266	0.072	-	-	-	-	-	-	-	-	-		
DOS		0.859	1.892	-0.694	0.102	0.862	1.367	-0.268	0.059	-	-	-	-	-	-	-	-	-		
FLAASH		0.869	1.793	-0.592	0.096	0.865	1.451	-0.290	0.082	-	-	-	-	-	-	-	-	-		
	Site 3										Site 4									
	Landsat 8 OLI vs. GOCI					Landsat 7 ETM+ vs. GOCI					Landsat 8 OLI vs. GOCI					Landsat 7 ETM+ vs. GOCI				
	n	R ²	a	b	RMSD	R ²	a	b	RMSD	n	R ²	a	b	RMSD	R ²	a	b	RMSD		
TOA	654	0.719	0.924	-0.025	0.130	0.662	0.844	0.006	0.122	2392	0.625	0.750	0.128	0.092	0.505	0.622	0.168	0.148		
6S		0.713	1.031	-0.037	0.123	0.659	0.997	0.059	0.128		0.658	0.924	0.083	0.075	0.536	0.735	0.224	0.083		
DOS		0.709	0.939	0.019	0.112	0.660	0.903	0.160	0.154		0.636	0.816	0.162	0.072	0.526	0.693	0.253	0.084		
FLAASH		0.706	1.023	-0.022	0.124	0.621	1.045	0.055	0.152		0.632	0.902	0.094	0.076	0.516	0.807	0.181	0.095		

It is noticeable that water NDVI from Landsat 8 OLI reflectance was much lower than that from Landsat 7 ETM+ reflectance (negative MBE in Fig. 5e, especially at sites 1 and 2). Further examination revealed significantly higher aerosol optical thickness on the day of Landsat 8 OLI image acquisition compared to Landsat 7 ETM+ acquisition (1.4 km compared to 0.15 km at site 1 and 1.05 km compared to 0.05 km at site 2), which was shown to result in lower water NDVI from MODTRAN simulation and 6SV atmospheric correction (Fig. 4d).

4.3. Comparisons with MODIS, GOCI and LED NDVI

The comparisons between Landsat 8 OLI and Landsat 7 ETM+ NDVI and the same-day MODIS NDVI are shown in Fig. 7. A total of 665, 1887, 654 and 2392 500 m-resolution pixels were extracted at study sites 1–4, respectively. Both Landsat 8 OLI and Landsat 7 ETM+ NDVIs derived from atmospherically corrected surface reflectance agreed well with the same-day MODIS NDVI, with the mean bias within ±0.05 (Fig. 7a) and R² over 0.85 (Table 5). The variation of the NDVI bias was within 0.1 except that from TOA reflectance at site 3, where haze was significant. Statistical analysis showed that in most cases Landsat 8 OLI produced significantly smaller NDVI discrepancy (i.e., mean absolute difference) than Landsat 7 ETM+ with MODIS as reference (Fig. 7). The Landsat 8 OLI NDVI also had marginally better linear correlation with MODIS, i.e., greater R² and lower RMSD than Landsat 7 ETM+ (Table 5). For example, at site 1, the R² of the linear fit between Landsat 8 OLI and MODIS NDVI is consistently higher than that between Landsat 7 ETM+ and MODIS NDVI (Fig. 7). However, at the low range of NDVI, the Landsat 7 ETM+ NDVI agreed with MODIS NDVI better than Landsat 8 OLI. The latter produced substantially lower NDVI than MODIS. Similarly, as shown in Fig. 3, atmospheric correction methods dramatically reduced the bias between Landsat and MODIS NDVI compared to TOA reflectance-derived NDVI.

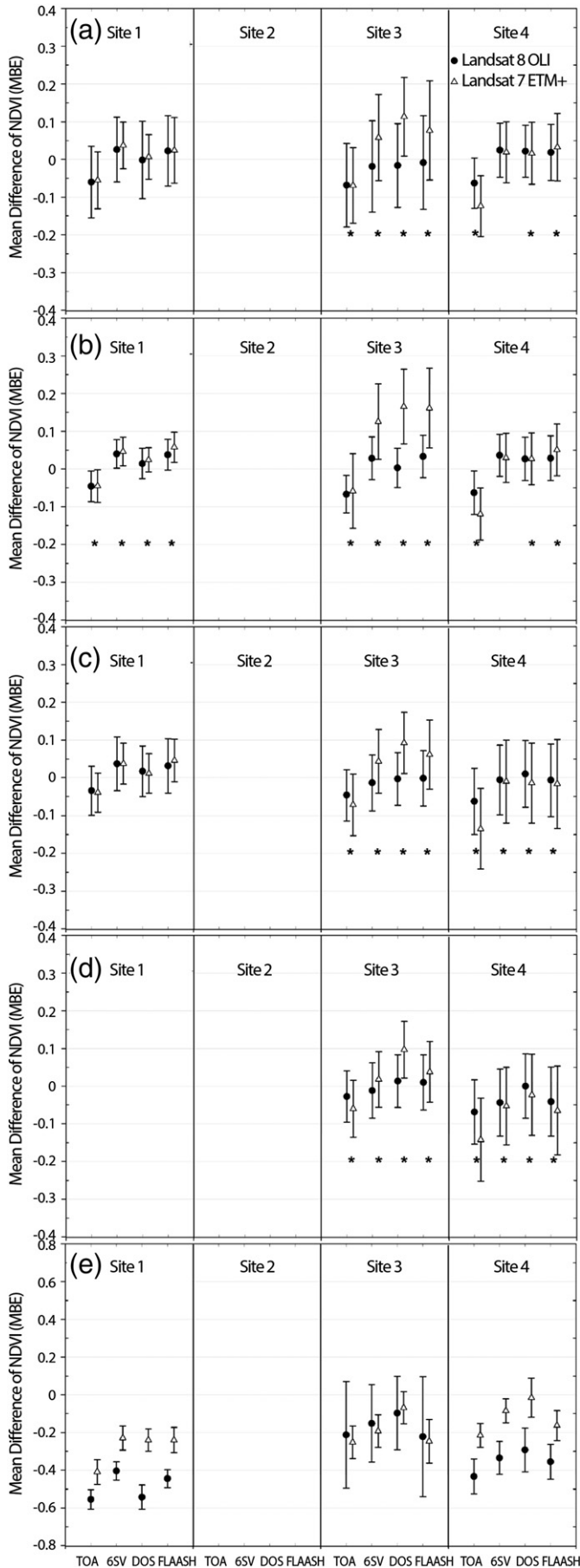
For vegetated areas such as forest and crop, the Landsat surface reflectance-derived NDVI and MODIS NDVI showed good agreement, with mean bias less than ±0.05, which was consistent with the simulation results. It can be found in Fig. 7b that at the forested area the bias of Landsat 8 OLI NDVI had slightly smaller dispersion than that of Landsat 7 ETM+ NDVI, suggesting that Landsat 8 OLI NDVI was more precise and better agreed with MODIS than Landsat 7 over vegetated surfaces. The lower dispersion between Landsat 8 OLI and MODIS may be attributed to higher SNR performance of the new instrument (222 at red band and 199 at NIR band) compared to Landsat 7 ETM+ instrument (26 at

red band and 34 at NIR band) (http://ldcm.nasa.gov/spacecraft_instruments/oli_perf.html). The SNR is also more comparable with MODIS instrument (128 at red band and 201 at NIR band) (<http://modis.gsfc.nasa.gov/about/specifications.php>), so that Landsat 8 OLI-derived NDVI is more precise. There were only 2, 3, and 6 urban pixels at sites 1, 2 and 4, respectively. At site 3, Landsat 8 OLI NDVI within urban area (n = 250) had better agreement with MODIS NDVI except for those derived from DOS corrected surface reflectance.

Within water area, the agreement between Landsat 8 OLI and MODIS NDVI was worse than that between Landsat 7 ETM+ and MODIS NDVI except at site 3. At sites 1, 2, and 4, because of MODIS Terra calibration errors on the day of Landsat 8 OLI acquisition, MODIS Terra data within ±2 days were used. Different atmospheric conditions could lead to considerable difference in water NDVI, which could explain the worse agreement of Landsat 8 OLI water NDVI than Landsat 7 ETM+ with MODIS. High water turbidity might decrease the water NDVI difference between Landsat 8 OLI and MODIS, which possibly increased NIR reflectance due to high concentration of suspended sediments thus relatively smaller difference in NDVI between the two sensors. Estuaries in site 3 are known to be turbid due to shallow bathymetry, strong tidal currents, and significant amounts of sediment coming from upstream (Kim, Im, Ha, Choi, & Ha, 2014). Weather records also show that there were heavy rains between 10 and 14 September 2013, which possibly contributed to turbid water in site 3. For all study sites, 6SV, and FLAASH atmospheric correction methods that are based on radiation transfer models yielded better agreement between Landsat and MODIS NDVIs, with generally smaller mean and standard deviation of the biases and higher R² (Table 5). Although the 6SV models used for Landsat atmospheric correction were similar as those used for MODIS surface reflectance product generation, FLAASH atmospheric correction methods did not result in significantly different Landsat NDVIs from MODIS. However, linear models between 6S-corrected Landsat NDVI and MODIS NDVI yielded slightly better goodness-of-fit and lower RMSD than those between FLAASH Landsat NDVI and MODIS NDVI. This suggests that 6SV atmospheric correction methods are preferred when Landsat NDVI is used in conjunction with MODIS NDVI. For consistency with the atmospheric correction methods used for MODIS generation, other methods based on radiative transfer models are also sufficient and should be used rather than image-based methods such as DOS.

Fig. 8 shows the comparisons between Landsat and GOCI NDVI at sites 1, 3, and 4 as site 2 is not covered by GOCI data. For consistency

Fig. 8. Scatter plots of Landsat 8 OLI and Landsat 7 ETM+ NDVI versus same-day MODIS NDVI at site 1 based on reflectance derived from (a)–(b) TOA radiance; (c)–(d) 6SV atmospheric correction; (e)–(f) DOS atmospheric correction and (g)–(h) FLAASH atmospheric correction methods. Left column: Landsat 8 OLI NDVI versus MODIS NDVI; right column: Landsat 7 ETM+ NDVI versus MODIS NDVI. The solid lines show linear regression model fits of the NDVIs. The dashed lines are 1:1 lines for reference. The color of the points illustrate the frequency of the NDVI values (red most frequent, blue least frequent).



with Landsat-MODIS comparison, surface reflectance from GOCI images was calculated using MODIS-based 6SV radiative transfer code. The mean NDVI differences between Landsat and GOCI NDVI were within 0.1 except for that between DOS-corrected Landsat 7 ETM+ and GOCI NDVI at site 3 (Fig. 8a). Compared to the differences between Landsat and MODIS NDVI, the Landsat-GOCI NDVI bias was overall greater and had considerably bigger variation. R^2 values of the Landsat-GOCI linear regression models ranged from 0.51 to 0.87, lower than that of the Landsat-MODIS linear models (Table 6 and Fig. 8) and the RMSD values of the models ranged from 0.05 to 0.15 (Table 6). At site 1, R^2 values of the linear models between Landsat and GOCI decreased from over 0.94 (Table 5) to around 0.87 when GOCI NDVI was used as reference (Table 6). It was also found that the Landsat 8 OLI and Landsat 7 ETM+ NDVI were higher than GOCI NDVI except in the lower range which corresponds to water area (Fig. 9). In the study by Yeom and Kim (2013) that evaluated the feasibility of GOCI data for land applications, it was reported that RMSD between MODIS and GOCI NDVI was at least 0.126. In our study, we found better agreement between Landsat and GOCI. This may be attributed to the spatial variation and dynamic atmospheric parameters such as AOT and water vapor applied in the 6SV models that yielded more consistent NDVI with MODIS. At both sites 3 and 4, Landsat 8 OLI NDVI generally had noticeably better agreement (higher R^2 and lower RMSD) with MODIS than Landsat 7 ETM+; similar patterns were shown in Landsat-GOCI comparisons.

The comparisons of Landsat and in-situ NDVI observations measured by LED sensors are displayed in Fig. 10. At both sites, using uncorrected Landsat 7 OLI or Landsat 8 OLI TOA reflectance resulted in a large negative bias in NDVI estimation. Especially on 8 September 2013, both deciduous and evergreen forest sites showed very low NDVI from Landsat 7 ETM+, indicating strong atmospheric scattering and attenuation impact on at-sensor radiance acquisition. Examination of MODIS atmosphere products showed high content of water vapor and aerosol optical thickness on that date compared to 16 September 2013, with water content approximately 2.01 g/cm² compared to 1.02 g/cm², and aerosol optical thickness around 0.62 km compared to 0.028 km. Atmospheric correction significantly reduced the NDVI error. At the deciduous forest site, both Landsat 7 ETM+ and Landsat 8 OLI NDVI derived by atmospherically corrected surface reflectance agreed well with the LED observations, with NDVI differences less than 0.05, except for an overestimation of 0.07 resulting from 6SV correction on Landsat 7 ETM+ on 8 September 2013. MODIS and GOCI also showed good agreement with LED NDVI. Unlike the deciduous forest site where tree species were homogenous within the Landsat and MODIS pixels, the coniferous site was more spatially heterogeneous and single Landsat and MODIS pixels contained mixed deciduous and evergreen trees (Ryu et al., 2014). Therefore, NDVIs were overestimated in Landsat, MODIS, and GOCI pixels. Nonetheless, at both sites, Landsat 8 OLI tends to produce more consistent NDVI values regardless of atmospheric correction methods used.

4.4. Spatial variability of Landsat 8 OLI NDVI

Landsat 30 m NDVI pixels were aggregated to 90 m, 150 m, 300 m, and 500 m grids, and the mean standard deviation within the new grids was calculated to represent the spatial variability of the NDVIs. For brevity, Fig. 11 only demonstrates the spatial variability of NDVI derived from the 6S corrected surface reflectance. Since different atmospheric correction methods produced similar NDVI results (Sections 4.2 and 4.3), it is reasonable to assume that the spatial variability of NDVIs from DOS and FLAASH methods have similar pattern as shown in Fig. 11.

Fig. 9. The mean NDVI differences between Landsat 8 OLI/Landsat 7 ETM+ and GOCI. The error bars show the standard deviation of the differences. (a) Overall; (b) forest; (c) crop; (d) urban; (e) water. Site 2 is excluded as GOCI does not cover the site. No information was given due to few urban samples for site 1 in (d). * denotes rejection of null hypothesis of mean absolute differences between Landsat 8 OLI and GOCI NDVI greater than or equal to that between Landsat 7 ETM+ and GOCI NDVI.

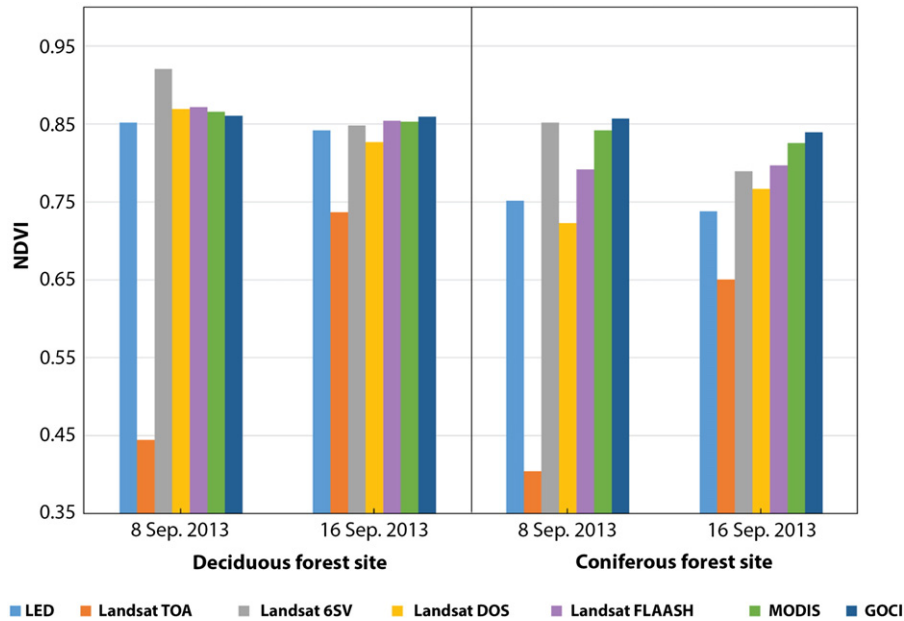


Fig. 10. NDVI generated from LED sensors, Landsat 7 and 8, MODIS, and GOCI instruments on 8 (Landsat 7 ETM+) and 16 September 2013 (Landsat 8 OLI) at the deciduous forest site and coniferous forest site.

Both Landsat 8 OLI and Landsat 7 ETM+ NDVI at the four study sites showed increasing variability with expanding grid sizes. Compared to the forest land cover, crop, and urban areas in both Landsat 8 OLI and Landsat 7 ETM+ images showed a more significantly rising trend, indicating higher spatial heterogeneity of crop (and urban) NDVI with increasing grid size.

Overall, NDVI derived from Landsat 8 OLI sensor data shows greater spatial variability compared to that from Landsat 7 ETM+ (Fig. 11a). This pattern was more prominent for crop and urban areas where Landsat 8 OLI produced considerably higher mean standard deviation (Eq. 4) of NDVI than Landsat 7 ETM+. While in the forested area, this difference was not as apparent. Since crop and urban land cover types typically show greater heterogeneity than the forested area, the increased spatial variability of Landsat 8 OLI NDVI proved that the new Landsat sensor has better capability of capturing small diversities of land surface characteristics, which may be attributed to greater SNR and the radiometric sensitivity. The Landsat 8 OLI instrument is designed to have tens of thousands of highly sensitive detectors. It was found that the detectors are so sensitive that tiny discrepancies in radiance measurements are evident in dark, uniform areas such as large expanses of water (USGS Landsat mission headline, February 14, 2014, <http://landsat.usgs.gov/>). Nonetheless, the present study found that the standard deviation of Landsat 8 OLI NDVI was lower than that of Landsat 7 ETM+ within uniform water at sites 1, 2 and 4. At site 3, Landsat 8 OLI revealed higher spatial variability of turbid water that was not shown in Landsat 7 ETM+ imagery. The negative differences between Landsat 8 OLI and Landsat 7 ETM+ water NDVI reported in Section 4.3 and the invariant NDVI values both indicate that Landsat 8 OLI NDVI has better capability to identify water area.

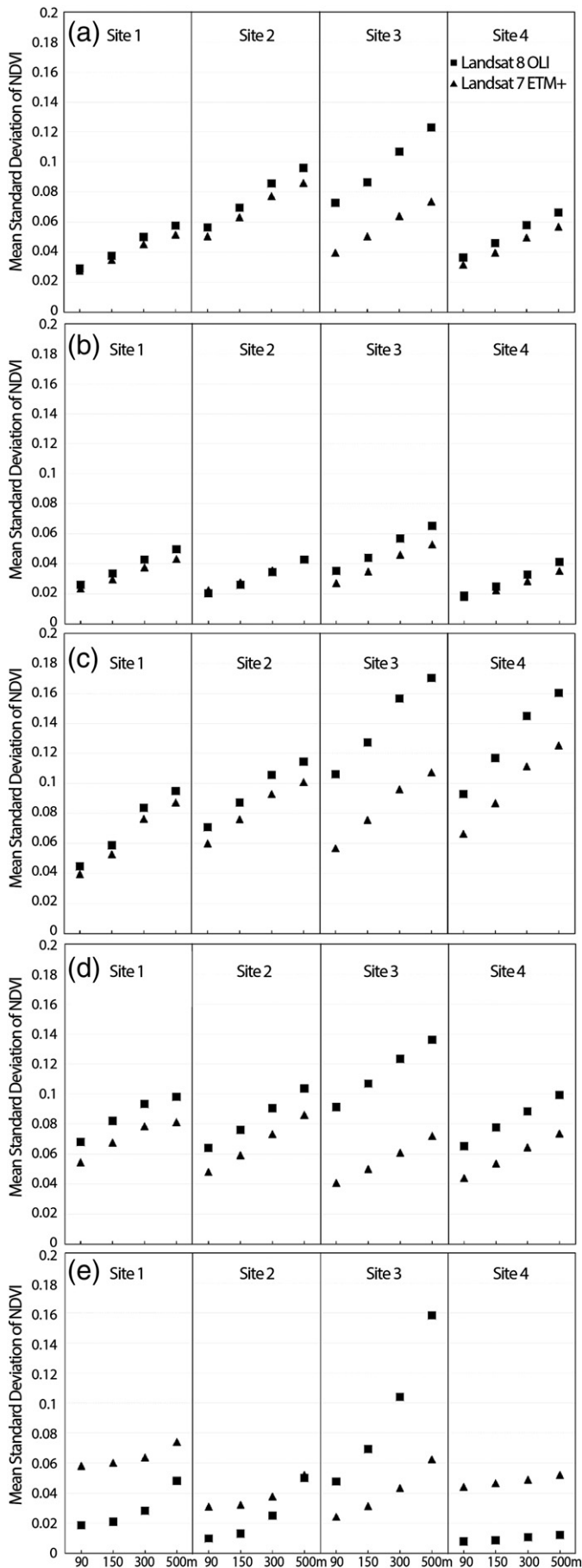
5. Conclusion

In this study, the characteristics of NDVI from the new instrument Landsat 8 OLI were investigated in terms of the consistency with Landsat 7 ETM+, MODIS, GOCI, and in-situ LED-derived NDVIs, and its spatial variability. Simulations of TOA and surface reflectance were conducted and the simulated NDVI were compared in order to assess the effect of band pass difference of the new instrument on NDVI calculation. Four study sites in China and Korea with an average area of 1928 km²

during leaf-on growing season with minimum cloud cover were examined, and NDVIs from TOA reflectance and surface reflectance by 6SV, DOS, and FLAASH atmospheric correction methods for each of the forest, crop, urban, and water land cover types were derived and compared.

The simulation results showed that Landsat 8 OLI, Landsat 7 ETM+, and MODIS NDVIs agreed well given the same atmospheric condition, while aerosol optical depth was a major factor influencing NDVI, especially for water. The results from the four study sites were consistent with the simulation results. Given the same atmospheric correction methods applied to derive surface reflectance, Landsat 8 OLI and Landsat 7 ETM+ NDVIs had overall good agreement, with mean bias errors within ± 0.05 , the standard deviations of errors < 0.1 , and R^2 from 0.84 to 0.98. Both datasets had reasonable agreement with the same-day MODIS and GOCI NDVI, with the mean bias within ± 0.05 and ± 0.1 respectively. Both datasets also showed good agreement with in-situ LED NDVI measurements at homogeneous deciduous site, with the bias error within ± 0.07 . Regardless of the type of reference data, using NDVIs derived from TOA reflectance significantly increased the measurement errors, indicating the necessities of atmospheric correction prior NDVI calculation. Vegetated areas had better NDVI agreement than non-vegetated surfaces. Particularly, water NDVI from Landsat 8 OLI was considerably lower than that from Landsat 7 ETM+ due to the narrower near-infrared band at the longer center wavelength, which can assist in distinguishing water bodies and may help assess vegetation water content.

In the present study, we found that Landsat 8 OLI NDVI produced more precise agreement with MODIS and GOCI NDVI at vegetated areas. Landsat NDVIs from 6SV and FLAASH atmospheric correction methods that are based on radiative transfer models had better agreement with MODIS NDVI compared to DOS methods. In addition, Landsat 8 OLI produced considerably greater spatial variability of NDVIs than Landsat 7 ETM+ within heterogeneous land cover types such as crop, urban, and turbid water areas. NDVIs in clear water area, in contrast, have smaller spatial variability. Such characteristics, mainly associated with higher SNR performance and radiometric sensitivity of Landsat 8 OLI instrument, suggest a greater potential for the use of Landsat 8 OLI in land surface process monitoring such as land cover mapping and change detection, vegetation growth, and ET analysis. In addition, many environmental models that have used Landsat



TM/ETM+-derived NDVI such as energy balance models (e.g., SEBAL and METRIC) may require new parameterization on Landsat 8 OLI-derived NDVI based on its characteristics compared to the TM/ETM+ and NDVI.

Acknowledgment

This research was supported by National Space Lab Program and Basic Science Research Program through the National Foundation of Korea (NRF) funded by the Ministry of Science, ICT, & Future Planning (Grant: NRF-2013M1A3A3A02042391; NRF-2013R1A1A1009459), National Science Foundation of China (Grant: 41401493; 41130744), 2015 Beijing Nova Program (Grant: xx2015B060) and Beijing Overseas Talent Pool Program (Grant: BHTO201410062-QN). We thank Galam Lee and Chongya Jiang for maintaining LED-sensors.

References

- Bhatti, S., & Tripathi, N. (2014). Built-up area extraction using Landsat 8 OLI imagery. *GIScience and Remote Sensing*, 51, 445–467.
- Black, A., & Stephen, H. (2014). Relating temperature trends to the normalized difference vegetation index in Las Vegas. *GIScience and Remote Sensing*, 51, 468–482.
- Brown, M.E., Pinzón, J.E., Didan, K., Morisette, J.T., & Tucker, C.J. (2006). Evaluation of the consistency of long-term NDVI time series derived from AVHRR, SPOT-Vegetation, SeaWiFS, MODIS, and Landsat ETM+ sensors. *IEEE Transactions on Geoscience and Remote Sensing*, 44(7), 1787–1793.
- Chander, G., Markham, B., & Helder, D. (2009). Summary of current radiometric calibration coefficients for Landsat MSS, TM, ETM+, and EO-1 ALI sensors. *Remote Sensing of Environment*, 113, 893–903.
- Chavez, P. S. (1988). An improved dark-object subtraction technique for atmospheric scattering correction of multispectral data. *Remote sensing of environment*, 24(3), 459–479.
- Chen, C., Chen, C.R., & Son, N. (2012). Investigating rice cropping practices and growing areas from MODIS data using empirical mode decomposition and support vector machines. *GIScience and Remote Sensing*, 49, 117–138.
- Cheret, V., & Denux, J. (2011). Analysis of MODIS NDVI time series to calculate indicators of Mediterranean forest fire susceptibility. *GIScience and Remote Sensing*, 48, 171–194.
- De Beurs, K.M., & Henebry, G.M. (2004). Land surface phenology, climatic variation, and institutional change: Analyzing agricultural land cover change in Kazakhstan. *Remote Sensing of Environment*, 89(4), 497–509.
- Ding, Y., Zhao, K., Zheng, X., & Jiang, T. (2014). Temporal dynamics of spatial heterogeneity over cropland quantified by time-series NDVI, near infrared and red reflectance of Landsat 8 OLI imagery. *International Journal of Applied Earth Observation and Geoinformation*, 30, 139–145.
- Feng, M., Huang, C., Channan, S., Vermote, E.F., Masek, J.G., & Townshend, J.R. (2012). Quality assessment of Landsat surface reflectance products using MODIS data. *Computers & Geosciences*, 38(1), 9–22.
- Gao, Z., Wang, Q., Cao, X., & Gao, W. (2014). The responses of vegetation water content (EWT) and assessment of drought monitoring along a coastal region using remote sensing. *GIScience and Remote Sensing*, 51, 1–16.
- GIS Ag Maps (2014). www.gisagmaps.com/ (last accessed: November 6th, 2014).
- Glenn, E.P., Huete, A.R., Nagler, P.L., & Nelson, S.G. (2008). Relationship between remotely-sensed vegetation indices, canopy attributes and plant physiological processes: What vegetation indices can and cannot tell us about the landscape. *Sensors*, 8, 2136–2160.
- Gong, B., Im, J., Jensen, J., Coleman, M., Rhee, J., & Nelson, E. (2012). Characterization of forest crops with a range of nutrient and water treatments using AISA hyperspectral imagery. *GIScience and Remote Sensing*, 49, 463–497.
- Gong, P., Wang, J., Yu, L., Zhao, Y.C., Zhao, Y.Y., Liang, L., et al. (2013). Finer resolution observation and monitoring of global land cover: First mapping results with Landsat TM and ETM+ data. *International Journal of Remote Sensing*, 34, 2607–2654.
- Hadjimitsis, D.G., Papadavid, G., Agapiou, A., Themistocleous, K., Hadjimitsis, M.G., Retalis, A., et al. (2010). Atmospheric correction for satellite remotely sensed data intended for agricultural applications: Impact on vegetation indices. *Natural Hazards and Earth System Sciences*, 10(1), 89–95.
- Hielkema, J.U., Prince, S.D., & Astle, W.L. (1986). Rainfall and vegetation monitoring in the savanna zone of the Democratic Republic of Sudan using the NOAA Advanced Very High Resolution Radiometer. *International Journal of Remote Sensing*, 7(11), 1499–1513.
- Hong, S.H., Hendrickx, J.M., & Borchers, B. (2009). Up-scaling of SEBAL derived evapotranspiration maps from Landsat (30 m) to MODIS (250 m) scale. *Journal of Hydrology*, 370(1), 122–138.
- Im, J., Lu, Z., Rhee, J., & Jensen, J.R. (2012a). Fusion of feature selection and optimized immune networks for hyperspectral image classification of urban landscapes. *Geocarto International*, 27, 373–393.

Fig. 11. Mean standard deviation of 6S-derived NDVI within 90 m, 150 m, 300 m, and 500 m grids. Squared symbol denotes Landsat 8 OLI and triangle symbol denote Landsat 7 ETM+. (a) Overall; (b) forest; (c) urban; (d) crop; (e) water.

- Im, J., Lu, Z., Rhee, J., & Quackenbush, L.J. (2012b). Impervious surface quantification using a synthesis of artificial immune networks and decision/regression trees from multi-sensor data. *Remote Sensing of Environment*, 117, 102–113.
- Ju, J., Roy, D., Vermote, E., Masek, J., & Kovalsky, V. (2012). Continental-scale validation of MODIS-based and LEDAPS Landsat ETM+ atmospheric correction methods. *Remote Sensing of Environment*, 122, 175–184.
- Kim, Y., Im, J., Ha, H., Choi, J., & Ha, S. (2014). Machine learning approaches to coastal water quality monitoring using GOCI satellite data. *GIScience and Remote Sensing*, 51, 158–174.
- Kleynhans, W., Olivier, J.C., Wessels, K.J., Salmon, B.P., Van den Bergh, F., & Steenkamp, K. (2011). Detecting land cover change using an extended Kalman filter on MODIS NDVI time-series data. *IEEE Geoscience and Remote Sensing Letters*, 8(3), 507–511.
- Lambert, J., Drenou, C., Denux, J., Balent, G., & Cheret, V. (2013). Monitoring forest decline through remote sensing time series analysis. *GIScience and Remote Sensing*, 50, 437–457.
- Li, M., Im, J., & Beier, C. (2013). Machine learning approaches for forest classification and change analysis using multi-temporal Landsat TM images over Huntington Wildlife Forest. *GIScience and Remote Sensing*, 50, 361–384.
- Li, P., Jiang, L., & Feng, Z. (2014). Cross-comparison of vegetation indices derived from Landsat-7 Enhanced Thematic Mapper Plus (ETM+) and Landsat-8 Operational Land Imager (OLI) sensors. *Remote Sensing*, 6, 310–329.
- Liu, Y., Wang, X., Tani, H., Matsuoka, N., & Matsumura, S. (2011). Spatial and temporal relationships among NDVI, climate factors, and land cover changes in Northeast Asia from 1982 to 2009. *GIScience and Remote Sensing*, 48, 371–393.
- Lunetta, R.S., Knight, J.F., Ediriwickrema, J., Lyon, J.G., & Worthy, L.D. (2006). Land-cover change detection using multi-temporal MODIS NDVI data. *Remote Sensing of Environment*, 105(2), 142–154.
- Maiersperger, T.K., Scaramuzza, P.L., Leigh, L., Shrestha, S., Gallo, K.P., Jenkerson, C.B., et al. (2013). Characterizing LEDAPS surface reflectance products by comparisons with AERONET, field spectrometer, and MODIS data. *Remote Sensing of Environment*, 136, 1–13.
- Masek, J. G., Vermote, E. F., Saleous, N. E., Wolfe, R., Hall, F. G., Huemmrich, K. F., et al. (2006). A Landsat surface reflectance dataset for North America, 1990–2000. *IEEE Transactions on Geoscience and Remote Sensing Letters*, 3(1), 68–72.
- Meng, Q., Cooke, W., & Rodgers, J. (2013). Derivation of 16-day time-series NDVI data for environmental studies using a data assimilation approach. *GIScience and Remote Sensing*, 50, 500–514.
- Ozdemir, I. (2014). Linear transformation to minimize the effects of variability in understory to estimate percent tree canopy cover using RapidEye data. *GIScience and Remote Sensing*, 51, 288–300.
- Pervez, S., Budde, M., & Rowland, J. (2014). Mapping irrigated areas in Afghanistan over the past decade using MODIS NDVI. *Remote Sensing of Environment*, 149, 155–165.
- Rhee, J., Im, J., & Carbone, G.J. (2010). Monitoring agricultural drought for arid and humid regions using multi-sensor remote sensing data. *Remote Sensing of Environment*, 114, 2875–2887.
- Roy, D., Wulder, M., Loveland, T., Woodcock, C., Allen, R., Anderson, M., et al. (2014). LANDSAT-8: Science and product vision for terrestrial global change research. *Remote Sensing of Environment*, 145, 154–172.
- Ryu, Y., Baldocchi, D.D., Verfaillie, J., Ma, S., Falk, M., Ruiz-Mercado, I., et al. (2010). Testing the performance of a novel spectral reflectance sensor, built with light emitting diodes (LEDs), to monitor ecosystem metabolism, structure and function. *Agricultural and Forest Meteorology*, 150, 1597–1606.
- Ryu, Y., Kang, S., Moon, S.K., & Kim, J. (2008). Evaluation of land surface radiation balance derived from Moderate Resolution Imaging Spectrometer (MODIS) over complex terrain and heterogeneous landscape on clear sky days. *Agricultural and Forest Meteorology*, 148, 1538–1552.
- Ryu, Y., Lee, G., Jeon, S., Song, Y., & Kimm, H. (2014). Monitoring multi-layer canopy spring phenology of temperate deciduous and evergreen forests using low-cost spectral sensors. *Remote Sensing of Environment*, 149, 227–238.
- Teillet, P., & Ren, X. (2008). Spectral band difference effects on vegetation indices derived from multiple satellite sensor data. *Canadian Journal of Remote Sensing*, 34, 159–173.
- Tucker, C.J., Pinzon, J.E., Brown, M.E., Slayback, D.A., Pak, E.W., Mahoney, R., et al. (2005). An extended AVHRR 8-km NDVI dataset compatible with MODIS and SPOT vegetation NDVI data. *International Journal of Remote Sensing*, 26(20), 4485–4498.
- USGS (2013). http://landsat.usgs.gov/Landsat8_Using_Product.php last accessed on February 20th, 2015.
- Van Leeuwen, W.J., Orr, B.J., Marsh, S.E., & Herrmann, S.M. (2006). Multi-sensor NDVI data continuity: Uncertainties and implications for vegetation monitoring applications. *Remote Sensing of Environment*, 100(1), 67–81.
- Vermote, E.F., & Vermeulen, A. (1999). MODIS algorithm technical background document: Atmospheric correction algorithm: Spectral reflectances (MOD09). https://lpdaac.usgs.gov/products/modis_products_table/mod09ga (Last access: January 17, 2015).
- Yeom, J., & Kim, H. (2013). Feasibility of using Geostationary Ocean Colour Imager (GOCI) data for land applications after atmospheric correction and bidirectional reflectance distribution function modelling. *International Journal of Remote Sensing*, 34, 7329–7339.
- Yuan, F., Wang, C., & Mitchell, M. (2014). Spatial patterns of land surface phenology relative to monthly climate variations: US Great Plains. *GIScience and Remote Sensing*, 51, 30–50.
- Zhang, X., Friedl, M.A., Schaaf, C.B., Strahler, A.H., Hodges, J.C., Gao, F., et al. (2003). Monitoring vegetation phenology using MODIS. *Remote Sensing of Environment*, 84(3), 471–475.
- Zhu, Z., & Woodcock, C.E. (2012). Object-based cloud and cloud shadow detection in Landsat imagery. *Remote Sensing of Environment*, 118, 83–94.